A&A, 684, L22 (2024)
https://doi.org/10.1051/0004-6361/202449365

Astronomy & Astrophysics

LETTER TO THE EDITOR

Imaging spectroscopy of a spectral bump in a type II radio burst⋆

Peijin Zhang[1,2,3], Diana E. Morosan[1,4], Pietro Zucca[5], Sanna Normo[4], Bartosz Dabrowski[6], Andrzej Krankowski[6], and Christian Vocks[7]

[1] Department of Physics, University of Helsinki, PO Box 64, 00014 Helsinki, Finland
[2] Center for Solar-Terrestrial Research, New Jersey Institute of Technology, Newark, NJ, USA
e-mail: peijin.zhang@njit.edu
[3] Cooperative Programs for the Advancement of Earth System Science, University Corporation for Atmospheric Research, Boulder, CO, USA
[4] Department of Physics and Astronomy, University of Turku, 20500 Turku, Finland
e-mail: diana.morosan@utu.fi
[5] ASTRON – the Netherlands Institute for Radio Astronomy, Oude Hoogeveensedijk 4, 7991 PD Dwingeloo, The Netherlands
[6] Space Radio-Diagnostics Research Centre, University of Warmia and Mazury, R. Prawochenskiego 9, Olsztyn 10-719, Poland
[7] Leibniz-Institut für Astrophysik Potsdam (AIP), An der Sternwarte 16, 14482 Potsdam, Germany

Received 27 January 2024 / Accepted 28 March 2024

ABSTRACT

Context. Observations of solar, type II radio bursts provide a unique opportunity to analyze the nonthermal electrons accelerated by coronal shocks and diagnose the plasma density distribution in the corona. However, there are very few high-frequency resolution interferometric observations of type II radio bursts that are capable of tracking these electrons.
Aims. Recently, more spatially resolved high-resolution observations of type II radio bursts have been recorded with the Low-Frequency Array (LOFAR). Using these observations, we aim to track the location of a type II radio burst that experienced a sudden spectral bump.
Methods. We present the first radio imaging observations of a type II burst with a spectral bump. We measured the variation in source location and frequency drift of the burst and deducted the density distribution along its propagation direction.
Results. We have identified a type II burst that experiences a sudden spectral bump in its frequency-time profile. The overall frequency drift rate is 0.06 MHz s^{-1}, and this corresponds to an estimated speed of 295 km s^{-1}. The projected velocity of the radio source obtained from imaging is 380 km s^{-1} toward the east. At the spectral bump, a deviation in the source locations of the type II split bands is observed. The band separation increases significantly in the north–south direction.
Conclusions. The spectral bump shows an 8 MHz deviation at 60 MHz, which corresponds to a 25% decrease in the plasma density. The estimated crossing distance during the spectrum bump was 29 mm, suggesting that this density variation occurs in a confined area. This indicates that the shock most likely encountered the upper extent of a coronal hole.

Key words. Sun: corona – Sun: coronal mass ejections (CMEs) – Sun: radio radiation

1. Introduction

Solar radio bursts present a crucial diagnostic of the underlying acceleration processes and conditions in the solar atmosphere. These emissions can provide information on the energy release process in solar activities as well as diagnostics on the background plasma of the solar corona (Wild & McCready 1950). Solar radio bursts in the low-frequency radio range are categorized into five main types (types I–V) based on the dynamic spectrum morphology. These five types of radio emission correspond to different physical processes in the solar corona. Type II radio bursts are generally accepted to be associated with coronal shocks (e.g., Mann & Klassen 2005; Morosan et al. 2023; Ramesh et al. 2023).

Type II solar radio bursts are interpreted as the signature of shock-accelerated electron beams generating Langmuir waves close to the local plasma frequency (f_p) that are then converted into radio emission at a fundamental (F) and harmonic (H) frequency of f_p (e.g., Melrose 1980; Nelson & Melrose 1985; Cairns et al. 2003). The overall shape of a type II radio burst slowly drifts from high to low frequencies in the dynamic spectrum. Within this drifting feature, there are lots of other fine-structured features, which reflects the background density variation and/or electron beam properties (e.g., Cairns & Robinson 1987; Magdalenić et al. 2020; Morosan et al. 2019, 2024; Zhang et al. 2024). One such interesting feature is the short-term (approximately minute timescale) significant variation or jumps from the general direction of the drifting lane ($\Delta f/f \sim 10\%$, where f is the emission frequency). Previous observations of a spectral jump or bump (Koval et al. 2021; Feng et al. 2013) show that the frequency is offset toward a higher frequency, and this is attributed to the interaction of the shock with high-density structures (e.g., coronal streamers). Until now, there had been no radio imaging of spectral bumps to show the variation in location of the radio source when it experiences such a bump.

Radio imaging has emerged as an invaluable tool in the quest to understand these phenomena better. Unlike traditional spectrographs that provide only spectral information, radio imaging

⋆ Movie associated to Fig. 1 is available at https://www.aanda.org

can spatially resolve the source regions of these emissions. This spatial resolution is pivotal in tracing the origins, paths, and interactions with the ambient solar atmosphere of these radio waves. Recent advancements in radio telescope technology have markedly improved our understanding of type II radio burst properties, offering significant insights into their evolution. For example, Morosan et al. (2019) used tied-array beam imaging observations with the Low-Frequency Array (LOFAR) to image herringbone bursts and identified the presence of shock-accelerated electron beams at multiple regions around a coronal mass ejection (CME) shock. Maguire et al. (2021), using LOFAR interferometry imaging combined with extreme-ultraviolet observations, showed that a type II radio source is located above a solar jet, which suggests the burst source was generated by a jet-driven piston shock instead of a CME-driven shock wave. In another study, Bhunia et al. (2023) performed radio imaging with the Murchison Widefield Array (MWA) for a band-split type II burst at multiple frequencies, and found that the radio source is located at multiple locations close to the shock.

Despite the potential of radio imaging, there has been a distinct lack of high-quality imaging studies specifically targeted at type II radio bursts using modern interferometers. LOFAR (van Haarlem et al. 2013) is a radio telescope array with antenna stations spread across Europe. It operates at the lowest frequencies that can be observed from Earth, ranging from 10 to 240 MHz. The imaging capability provides the possibility of spatially resolving the radio signals from the coronal shock.

In this Letter, we aim to bridge this gap by presenting a comprehensive study using advanced interferometry imaging techniques. Section 2 presents the observation details, including data processing and an event overview. In Sect. 3 we explain our analysis of the type II bump, and Sect. 4 provides a discussion and our conclusions.

2. Observation

We carried out imaging and spectroscopy observations of a type II radio burst that occurred on May 23, 2022, at 11:25 UT (see Fig. 1); it has an identifier of `LT16_001` in the LOFAR long-term archive. The observation was carried out at 31 low band antenna LOFAR stations, of which 23 were core stations and 8 remote stations; the longest available baseline was 48 km. These 31 stations generated 496 station baselines. We used 60 frequency channels from 20 to 80 MHz, with a 195.3 kHz channel width. The time resolution of the imaging was 0.671 s. We used two simultaneous beams pointing at the Sun and a calibrator (Cassiopeia A). In the data processing steps, the calibrator was used to correct the phase and amplitude variations of the Sun observations. The dynamic spectrum was recorded by a stand-alone core station (CS032) with a time resolution of 10.5 ms and a frequency resolution of 12.5 kHz.

2.1. Data processing

The dynamic spectrum was preprocessed with a radio-frequency-interference-flagging tool for the solar and space weather spectrum, `ConvRFI`[1] (Zhang et al. 2023).

The interferometry data processing involved the following steps:

1. Gain calibration: For the calibrator observation, we computed the phase and amplitude offsets with a flux density model of the calibrator as a reference. This step generated a gain solution of phase and amplitude for each baseline and subband. The computation of the gain calibration was performed with `DP3`, the default preprocessing pipeline[2] (van Diepen et al. 2018).
2. Antenna inspection: We reviewed the phase and amplitude plots for each antenna and flagged corrupted data.
3. Applying the calibration: The gain solution was applied to the Sun observation to correct the phase and amplitude. This was also performed with `DP3`.
4. Imaging: We performed a 2D Fourier transform of the visibility map. Then, we executed the w-stacking CLEAN algorithm to de-convolute the point spread function from the image. The imaging step was performed with `wsclean`[3] (Offringa et al. 2014).
5. Postprocessing: We converted coordinates to helio-projective and the units to brightness temperature using `lofarSun`[4] (Zhang et al. 2022).

To characterize the spectroscopic features of the type II burst, we extracted the time and frequency evolution of each split band. We used a "smoothed line of local maximum" for the upper and lower bands (shown as green and blue lines in Fig. 1). Interferometric imaging was performed along the two bands, and we chose the closest available time-frequency points (shown as green and blue dots in Fig. 1).

2.2. The type II spectral bump

We show this type II solar radio burst in the dynamic spectrum in Fig. 1. The burst shows a fundamental–harmonic pair structure, with the fundamental starting near 35 MHz and the harmonic starting close to 70 MHz at ~11:25 UT. In the harmonic component of the type II burst, a notable anomaly appears as a distinctive "bump" within the frequency drift evolution. Here, the signal shifts toward lower frequencies by approximately 5−10 MHz, persisting for a duration of one minute before returning to the overall frequency drift evolution. Our analysis focuses on the imaging spectroscopy of the spectral bump. Thus, we focused on the spectral and spatial characteristics of the type II burst in the time range 11:25:00 UT to 11:30:30 UT. We categorized this 5.5-min time range into three phases: P1, P2, and P3, namely the periods before, during, and after the bump (see Fig. 1).

The type II burst shows band-splitting into two bands with a ~8 MHz frequency separation. We detected the band-split lanes by finding the local maxima on the upper and lower split bands. The upper panels of Fig. 1 present the full width at half maximum and peak location of the brightness temperature distribution of the higher-frequency band (HB; blue) and the lower-frequency band (LB; green) for P1, P2, and P3 in the dynamic spectrum.

3. Results

From the imaging along the type II bands, we can see that the source movement of the type II burst shows different behaviors during the P1, P2, and P3 phases, as shown in Fig. 2. The HB (blue) and LB (green) radio sources are separated in space vertically. During P1 and P3, the peak locations of the HB and LB sources both move from east to west, which indicates that the

[1] ConvRFI: https://github.com/peijin94/ConvRFI

[2] DP3: https://github.com/lofar-astron/DP3

[3] wsclean: https://gitlab.com/aroffringa/wsclean

[4] lofarSun: https://github.com/peijin94/LOFAR-Sun-tools

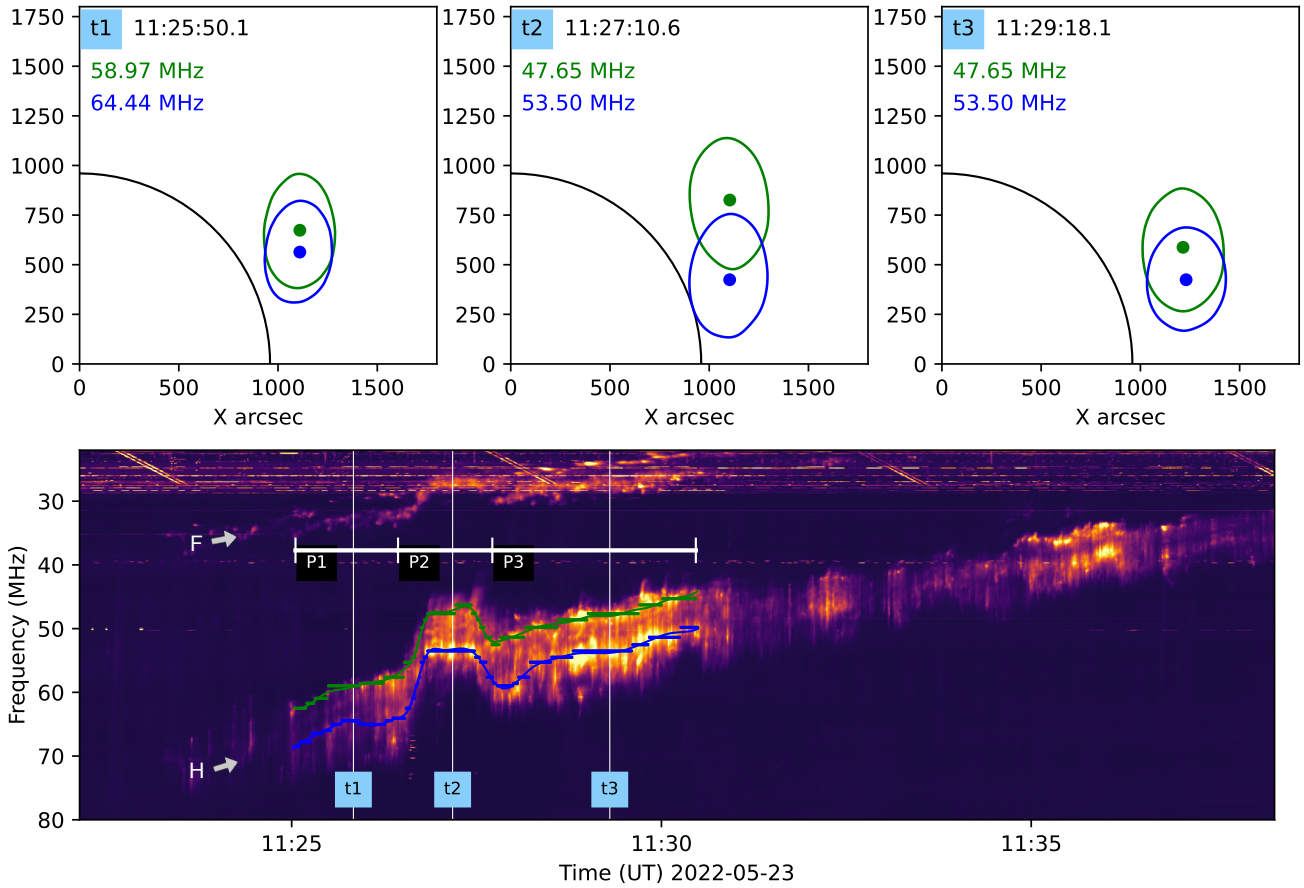

Fig. 1. Dynamic spectrum and imaging of three time-points in the type II radio burst. Blue represents the higher-frequency lane. The upper three panels show the source size and location at these three times, the dot marks the peak location, and the solid line marks the half-maximum contour. The solid black lines in the upper panel represent the solar disk. The lower panel shows the dynamic spectrum; the solid green and blue lines mark the upper and lower lane of the burst. The white horizontal lines mark the three phases of the burst: before the bump (P1), during the bump (P2), and after the bump (P3). The imaging of the three time slots (t1, t2, and t3) is presented in the upper three panels. F and H mark the fundamental and harmonic components in the dynamic spectrum. A related movie is available online.

shock is moving from east to west as well, as shown by the blue and green arrows in panels P1 and P3 of Fig. 2. However, during P2 (the time of the spectral bump), the upper and lower sources sharply separated in the north–south direction and stayed separated for ∼1 min before moving back closer to each other toward the end of the spectrum bump.

By fitting the source location variation with time, we measured its speed projected in the sky plane (see Fig. 3). During P1 and P3 (panels A and B in Fig. 3) the HB and LB sources have speeds in the x direction of 353 and 409 km s^{-1}, respectively, and y-direction speeds of −363 and −151 km s^{-1}. This indicates that the radio source motion is mostly from east to west, and partially to the south. With the average speed toward the west of 381 km s^{-1} and the 76-s duration of P2, we estimated the width of the density depletion to be 29 mm. During the spectral bump (phase P2), the source of both the HB and LB has a negative deviation from the movement trend of P1 and P3. In the x direction, this deviation is to the west. In the y direction, the source deviates toward the north for LB and toward the south for the HB, and the sources of the LB and HB converge back to the middle toward the end of the spectrum bump.

We estimated the heliocentric distance of the radio source from the frequency of the emission. To compare it with the source location from the imaging of the harmonic component in this type II burst, we assumed harmonic emission in the estimation $f = 2\omega_{\rm pe}$, where $\omega_{\rm pe}$ is the plasma frequency expressed as

$$\omega_{\rm pe} = \sqrt{\frac{N_{\rm e}(R)\, e^2}{m_{\rm e}\varepsilon_0}}.$$

Here $N_{\rm e}(R)$ is the background electron density from the empirical model (Saito et al. 1977). The result is shown in panel C of Fig. 3, where the higher and lower lanes have an estimated radial speed of 276 and 315 km s^{-1} in P1 and P3. The speed estimated from the empirical density model is slower by ∼100 km s^{-1} than the source motion speed obtained from imaging.

4. Discussion and conclusion

The observations and results of this study can be summarized as follows:

1. The "spectral bump" in the type II radio burst is 8 MHz at 60 MHz (for harmonic wave), which corresponds to a density drop of ∼25%.

2. The overall source moving trend is to the east (which corresponds to the shock preceding direction). The speed in the west–east direction is 408 km s^{-1} and 353 km s^{-1} as measured from the upper and lower lanes.

3. The distance the shock travels during the spectral bump is 29 mm, which is too small to be identified at other wavelengths. There are coronal holes near the western limb. There are also density fluctuations in the density model, but no direct counterpart can be found.

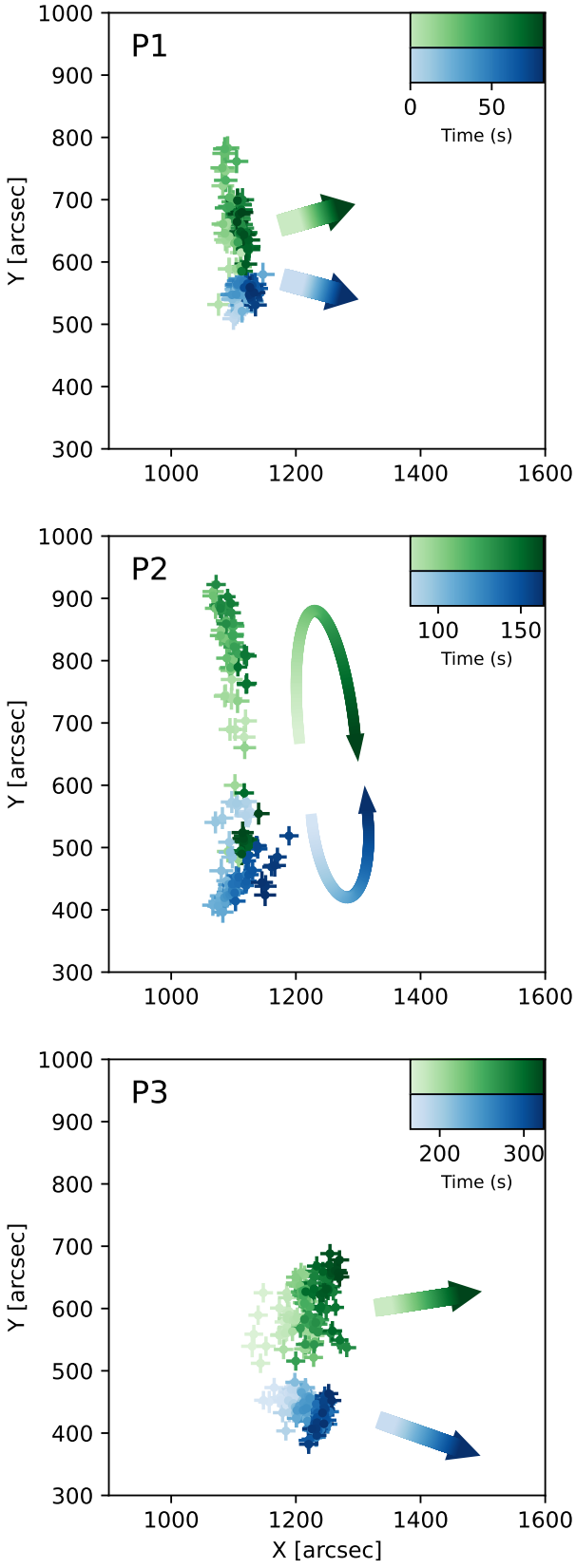

Fig. 2. Source location of the type II burst during the three phases. The points are colored according to time. The arrows indicate the source location variation trend.

4. At the peak of the bump, the source separation is ~500 arcsec to the northwest.

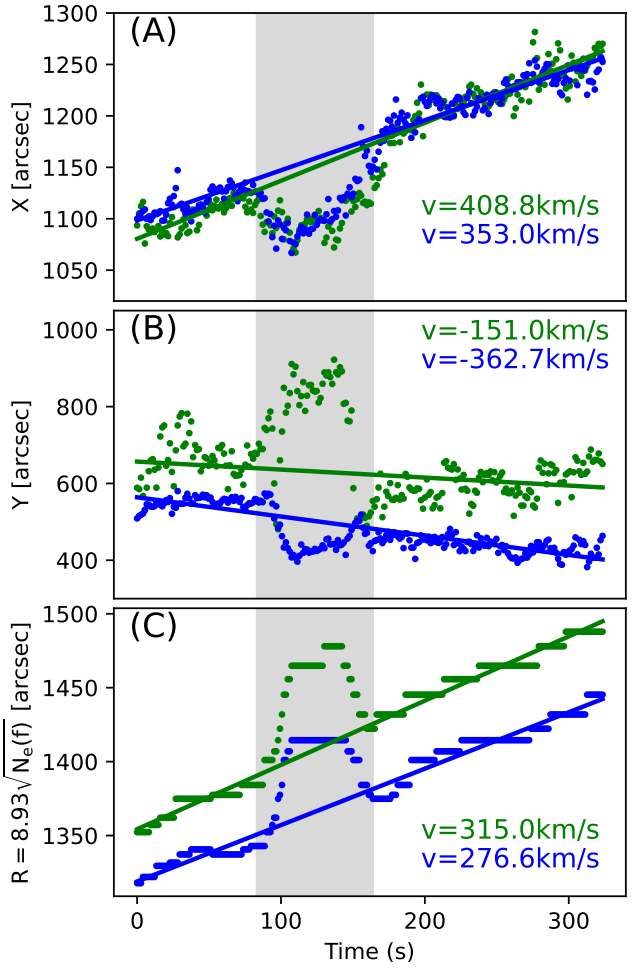

Fig. 3. Source location variations in the X and Y directions are shown in panels A and B. The heliocentric distance of the source derived from the frequency of the imaging is shown in panel C. The solid lines are the fitted result of the points in phase 1 and phase 3 (i.e., the points outside of the gray area).

Structures in type II radio bursts can reflect structures in the solar corona. The spectral bump analyzed in this work indicates that the shock encounters a compact, low-density region. We investigated extreme-ultraviolet images to identify if there is a possible coronal hole or a lower-density region in the direction of the type II propagation. There is indeed a small coronal hole with sharp boundaries rotating onto the western limb in images from the Atmospheric Imaging Assembly on board the Solar Dynamic Observatory (Pesnell et al. 2012). This coronal hole is clearly visible two to three days before the type II burst. However, it is hard to identify these coronal holes in the observations as they are located too close to the solar limb. It is possible that the low density and open magnetic field of a coronal hole can cause a spectral bump accompanied by a source separation when encountered by a shock. A cartoon of the source deviation is shown in Fig. 4. In this cartoon, the movement in the x direction can be explained by the source being emitted at farther locations along a curved shock front. The separation in the y direction is likely due to the shock encountering a density drop (such as a coronal hole boundary), which causes the emission to either shift or fan outward with the open coronal magnetic field lines originating from a coronal hole.

The observed spatial separation between the two bands also confirms the theory that band-splitting is caused by emission at

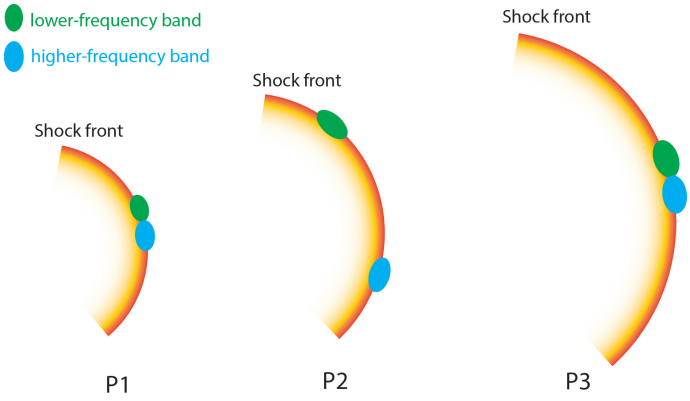

Fig. 4. Shock front evolution and relative source location. The red arc represents the shock front, and the blue and green regions mark the location of the radio source.

different locations upstream of the shock, as initially suggested by Holman & Pesses (1983). This is particularly clear during the spectral bump, where such a high separation (~500 arcsec, which corresponds to 0.5 $R_\odot$) cannot be attributed to radio propagation effects. The radio source location can be affected by propagation effects such as scattering and refraction. They can cause a 0.2 $R_{\rm sun}$ radial offset for a fundamental wave and a 0.05 $R_{\rm sun}$ offset for a harmonic wave for a 35 MHz radio source near the limb (Zhang et al. 2021). In the present study we only considered the harmonic emission of a type II burst at even higher frequencies and find a large separation of 0.5 $R_\odot$. Thus, propagation effects are most likely negligible in our case. The results of other recent studies have also been consistent with the Holman & Pesses (1983) theory of band-split emission, finding consistent separations of the split bands throughout the evolution of the type II burst, similar to our study (e.g., Bhunia et al. 2023; Morosan et al. 2023).

Acknowledgements. P.Z. and D.E.M. acknowledge the University of Helsinki Three-Year Grant. P.Z. is supported by the NASA Living With a Star Jack Eddy Postdoctoral Fellowship Program, administered by UCAR's Cooperative Programs for the Advancement of Earth System Science (CPAESS) under award NNX16AK22G. D.E.M. and S.N. acknowledge the Research Council of Finland project "SolShocks" (grant number: 354409). D.E.M. also acknowledges the Academy of Finland project "RadioCME" (grant number 333859). C.V. has been supported by the Deutsche Forschungsgemeinschaft (DFG, German Research Foundation) under project number VO 2123/1-1. The authors wish to acknowledge CSC – IT Center for Science, Finland, for computational resources. LOFAR (van Haarlem et al. 2013) is the Low Frequency Array designed and constructed by ASTRON. Data available at https://lta.lofar.eu/. The LOFAR ILT resources have benefited from the following recent major funding sources: CNRS-INSU, Observatoire de Paris and Université Orléans, France; BMBF, MIWF-NRW, MPG, Germany; Science Foundation Ireland (SFI), Department of Business, Enterprise and Innovation (DBEI), Ireland; NWO, The Netherlands; The Science and Technology Facilities Council, UK; The Ministry of Science and Higher Education (MEiN), Poland. U.W.M. thanks the National Science Centre, Poland for granting "LOFAR observations of the solar corona during Parker Solar Probe perihelion passages" in Beethoven Classic 3 funding initiative under project number 2018/31/G/ST9/01341. U.W.M. would also like to thank (MEiN) for its contribution to the ILT, LOFAR2.0 upgrade (decision numbers: 2021/WK/2, 30/530252/SPUB/SP/2022, 29/530358/SPUB/SP/2022, 28/530020/SPUB/SP/2022, respectively).

References

Bhunia, S., Carley, E., Oberoi, D., & Gallagher, P. 2023, A&A, 670, A169
Cairns, I. H., & Robinson, R. D. 1987, Sol. Phys., 111, 365
Cairns, I. H., Knock, S. A., Robinson, P. A., & Kuncic, Z. 2003, Space Sci. Rev., 107, 27
Feng, S. W., Chen, Y., Kong, X. L., et al. 2013, ApJ, 767, 29
Holman, G. D., & Pesses, M. E. 1983, ApJ, 267, 837
Koval, A., Karlický, M., Stanislavsky, A., et al. 2021, ApJ, 923, 255
Magdalenić, J., Marqué, C., Fallows, R. A., et al. 2020, ApJ, 897, L15
Maguire, C. A., Carley, E. P., Zucca, P., Vilmer, N., & Gallagher, P. T. 2021, ApJ, 909, 2
Mann, G., & Klassen, A. 2005, A&A, 441, 319
Melrose, D. B. 1980, Space Sci. Rev., 26, 3
Morosan, D. E., Carley, E. P., Hayes, L. A., et al. 2019, Nat. Astron., 3, 452
Morosan, D., Pomoell, J., Kumari, A., Kilpua, E., & Vainio, R. 2023, A&A, 675, A98
Morosan, D. E., Pomoell, J., Palmroos, C., et al. 2024, A&A, 683, A31
Nelson, G. J., & Melrose, D. B. 1985, in Solar Radiophysics: Studies of Emission from the Sun at Metre Wavelengths, eds. D. J. McLean, & N. R. Labrum, 333
Offringa, A. R., McKinley, B., Hurley-Walker, N., et al. 2014, MNRAS, 444, 606
Pesnell, W. D., Thompson, B. J., & Chamberlin, P. C. 2012, Sol. Phys., 275, 3
Ramesh, R., Kathiravan, C., & Kumari, A. 2023, ApJ, 943, 43
Saito, K., Poland, A. I., & Munro, R. H. 1977, Sol. Phys., 55, 121
van Diepen, G., Dijkema, T. J., & Offringa, A. 2018, Astrophysics Source Code Library [record ascl:1804.003]
van Haarlem, M. P., Wise, M. W., Gunst, A., et al. 2013, A&A, 556, A2
Wild, J. P., & McCready, L. L. 1950, Aust. J. Sci. Res. A Phys. Sci., 3, 387
Zhang, P., Wang, C., & Kontar, E. P. 2021, ApJ, 909, 195
Zhang, P., Zucca, P., Kozarev, K., et al. 2022, ApJ, 932, 17
Zhang, P., Offringa, A. R., Zucca, P., Kozarev, K., & Mancini, M. 2023, MNRAS, 521, 630
Zhang, P., Morosan, D., Kumari, A., & Kilpua, E. 2024, A&A, 683, A123